nature synthesis

Article

https://doi.org/10.1038/s44160-023-00401-8

Face-directed assembly of tailored isoreticular MOFs using centring structure-directing agents

Received: 23 May 2023

Accepted: 15 August 2023

Published online: 2 October 2023

Check for updates

Marina Barsukova[1], Aleksandr Sapianik[1], Vincent Guillerm[1] ✉, Aleksander Shkurenko[1], Aslam C. Shaikh[1], Prakash Parvatkar[1], Prashant M. Bhatt[1], Mickaele Bonneau[1], Abdulhadi Alhaji[1], Osama Shekhah[1], Salvador R. G. Balestra[2,3], Rocio Semino[2,4], Guillaume Maurin[2] & Mohamed Eddaoudi[1] ✉

Building blocks with low connectivity and no embedded directionality are prone to polymorphism, as demonstrated by the diversity of 4-connected zeolitic nets (>250). As a result, their deployment for design in reticular and isoreticular chemistries remains a challenge. However, the ability to control geometrical peculiarities offers potential to deviate from the assembly of default structures. Here we report the face-directed assembly of >20 isoreticular zeolite-like metal–organic frameworks (ZMOFs) by using polytopic expanding and tightening centring structure-directing agents (cSDAs). The cSDAs are selected with the appropriate geometrical coding information to alter and control the orientation of adjacent supermolecular building blocks. The ZMOFs have an underlying sodalite (**sod**) topology that is remarkably suited for the rational assembly of multinary materials. In addition to a variety of metal cations (In, Fe, Co and Ni), a diverse range of cSDAs (di-, tri-, tetra-, hexa-, pyridyl or imidazole) are used and combined. Our approach enables isoreticular possibilities at both extremities of the porous materials spectrum: In-**sod**-ZMOF-102 exhibits small pore aperture suitable for efficient separation, while Fe-**sod**-ZMOF-320 with 48-Å-wide mesopores exhibits high hydrogen uptake, methane storage working capacity and a high gravimetric working capacity for oxygen.

In chorus with the rapid development of reticular chemistry[1] and the field of metal–organic frameworks (MOFs), resulting in more than a hundred thousand crystal structures[2], researchers dedicated a particular attention to developing rational synthesis strategies allowing the assembly of MOFs with specific topologies of interest[3,4]. Along with the molecular building block (MBB) and supermolecular building block (SBB) approaches[5] giving access to topologies never observed before, researchers successfully targeted the assembly of MOFs with well-known underlying topologies, zeolitic nets[6,7]. These zeolite-like MOFs (ZMOFs) have proven their potential for

[1]Functional Materials Design, Discovery and Development Research Group, Advanced Membranes and Porous Materials Center, Division of Physical Sciences and Engineering, King Abdullah University of Science and Technology, Thuwal, Saudi Arabia. [2]ICGM, Université Montpellier, CNRS, ENSCM, Montpellier, France. [3]Department of Physical, Chemical and Natural Systems, Universidad Pablo de Olavide, Sevilla, Spain. [4]Physico-chimie des Electrolytes et Nanosystèmes Interfaciaux, CNRS, PHENIX, Sorbonne Université, Paris, France. ✉e-mail: vguillerm@protonmail.com; mohamed.eddaoudi@kaust.edu.sa

myriad applications, for example in biochemistry[8,9], catalysis[10,11], gas storage[12] and separation of hydrocarbons[13–15] among other gas mixtures of interest[16].

While it is recognized that highly connected nets are ideal targets for the successful practice of reticular chemistry[3], such observation consequently highlights remaining design challenges for nets with low connectivity. Indeed, the Reticular Chemistry Structure Resource (RCSR) database[17,18] contains 666 entries for assembling 4-connected (4-c) nodes together[3], more than 250 of which being zeolitic nets[19] or nets based on the assembly of tetrahedral nodes (diamond **dia**, quartz **qtz** and so on); moreover, researchers have enumerated over 2.6 million of plausible theoretical zeolitic nets[20,21]. Being at the forefront of ZMOFs design for more than 15 years, our group discovered an unprecedented zeolitic topology[22] and introduced various efficient strategies to achieve ZMOFs: highly coordinated metal ions[23], metal–organic cubes[24,25] and, recently, a cantellation strategy yielding the mesoporous zirconium-based sodalite (**sod**) ZMOFs[26].

From a topological point of view, some approaches such as single metal ions bridged by imidazolate linkers offer a wide structural diversity[27,28]. The downside of such structural richness is the proportional difficulty to control the topology due to a lack of directional constraint in the system, compromising the possibility to practice isoreticular chemistry, decorate and fine tune the pore system on-demand. Other approaches relying on additionally embedded coded information in the building blocks can promote a single topology over others, this time restricting structural diversity. For example, in MIL-100 (ref. 29) and MIL-101 (ref. 30), two ZMOFs with underlying **mtn** topology, the nature of their supertetrahedra (STs) forces their conformation in eclipsed fashion due to a trigonal prismatic corner sharing, with a TOT angle (terminology from zeolites, the angle between two tetrahedral Si through O bridges) close to 180° between adjacent tetrahedra, and dominant pentagonal windows[31]. This strategy has also been proven suitable for isoreticular chemistry, permitting access to mesoporous **mtn** materials with high pore volumes[32,33], atypical for ZMOFs with other topologies than **mtn**[34].

In this Article, we propose a versatile face-directed assembly strategy (Fig. 1) inspired by architecture techniques, combining the SBB approach with the use of various centring structure-directing agents (cSDAs). For the construction of arches, bridges, oculus windows and so on, architects have developed elaborated systems to overcome the laws of gravity, using wooden formworks (also named centring) that would both help support and shape the edifice. This approach permits to alter and control the TOT angle between adjacent STs and consequently deviate from the **mtn** topology of MIL-100 type of MOFs[29,32,35], a rarely observed feature[36–38].

Analysis of the targeted sodalite topology, a semi-regular net with transitivity (1121), recognized as the ideal target blueprint through a systematic analysis of the zeolitic nets contained in the RCSR (>3,000 nets)[17,18], International Zeolite Association (IZA) (>250 nets)[19] and Hypothetical Zeolites Structures[20,21] databases, allowed us to identify two types of cSDAs, namely expanding-cSDA (Fig. 1c) and tightening-cSDA (Fig. 1b) that can direct the desired MOF assembly by capping the two different types of window of the **sod** net (Fig. 2). Taking advantage of the dependency equations relating the sizes of the ligand and cSDA, we were able to assemble 21 isoreticular ZMOFs with underlying **sod** topology, among them Fe-**sod**-ZMOF-320 with 48-Å-wide mesopores, and a pore volume of 3.21 $cm^3\ g^{-1}$ (N_2, 77 K), reaching 160% of the pore volume of the most porous sodalite material so far[26]. Fe-**sod**-ZMOF-320 exhibits high O_2, CH_4 and H_2 uptakes and working capacities, placing it among the top-performing materials for gas storage applications.

Results and discussion

Topology databases survey

While **mtn** is recognized to be the default topology for assembling eclipsed tetrahedra/STs with a TOT angle close to 180° (ref. 31) (Supplementary Figs. 123 and 124), a survey of the zeolitic nets in the IZA[19], RCSR[18] and Deem[20] databases allowed us to identify, among more than 300,000 topologies, a curated set of nets combining the following (Supplementary Table 20):

(1) Eclipsed tetrahedra exclusively
(2) No more than three vertices (distinct nodes)
(3) Reasonably high TOT angles

As the only edge-transitive net in the list, the semi-regular sodalite topology (SOD, **sod**) appears as the most promising candidate compared with AST, RHO, LTA, NPT, SAS or RWY. Moreover, after the default MTN net, **sod** is the topology requiring the highest minimal TOT angle (161°), therefore limiting the stress on adjacent tetrahedra.

Introducing a geometry mismatch

The **mtn** net with transitivity (3432) has three faces (windows), two pentagonals and one hexagonal, forming two tiles (cages). Pentagonal faces are present on the two types of tile (and the dodecahedral tile is made of pentagonal faces, exclusively), thus making them the 'dominant' ones, governing the topology. Therefore, introducing a geometry mismatch[39] that would prevent the formation of such pentagonal windows during the MOF assembly appears to be a suitable way to deviate from the default **mtn** topology. This mismatch for **mtn** should be alongside with a (re)match to promote the targeted **sod** topology (which does not contain pentagonal windows). The **sod** net with transitivity (1121) (one node, one edge, two faces and one tile) offers two main routes (Fig. 2):

(1) Promoting the formation of square windows, imposing the contraction of the ring from 5-member ring (MR) to 4MR (Fig. 2b). In this case, tetratopic square ligands can be used as cSDAs.
(2) Promoting the formation of hexagonal windows, imposing the expansion of the ring from 5MR to 6MR (Fig. 2c). This can be achieved by introduction of di, tri, tetra or hexatopic cSDAs with an inner angle of 120° to 6MR in the structure.

The edge net (**sod-e**) reflects well the structure of sodalite zeolite and is obtained from the **sod** net by placing vertices in the middle of the edges, discarding the original vertices and edges, and joining the new vertices to enclose the coordination figure of the original vertices (Supplementary Fig. 75). The corresponding 4MR and 6MR faces of the **sod** net are now represented by sequences of 4 and 6 corner shared tetrahedra.

Identifying suitable building units

Overall, bringing closer (tightening) two opposite corners of adjacent tetrahedra permits to reduce from 5 to 4 the number of tetrahedra forming the window and form a 4MR window instead of a 5MR; this can be achieved by applying an additional force to reduce the TOT angle from the ideal 180° to approximately 160°, and the TTT angle from 108° in a pentagon to 90° in a square (Fig. 2b). To this end, a square tightening-cSDA can be used. In contrast, to obtain a 6MR window, one needs to increase from 5 to 6 the number of tetrahedra forming the window, by pushing further two opposite corners of adjacent tetrahedra (Fig. 2a). To this end, while a hexagonal expanding-cSDA would be ideal, trigonal, tetragonal or angular ditopic (120°) cSDAs should act similarly, meanwhile allowing more options with regard to organic MBB diversity (Fig. 1c). This corresponds to increasing the TOT angle from 180° to 199°, and the TTT angle from 108° in a pentagon to 120° in a hexagon.

The ability of pyridil or imidazole terminated ligands to connect trimeric MBBs through their open metal sites is known and makes these ligands ideal cSDAs for synthetic approach. The typical connectivity of 6 $[M_3(\mu_3\text{-}O)(O_2C\text{-}R)_6]$ in such MBBs can be extended up to 9 $[M_3(\mu_3\text{-}O)(O_2C\text{-}R)_6)(N\text{-}R')_3]$ (ref. 40), allowing for the required range of connectivity.

Vertex dependency equations

To find the suitable cSDA linkers fitting square or hexagonal windows of the targeted ZMOFs, the analysis of general ST structure and resulting

https://doi.org/10.1038/s44160-023-00401-8

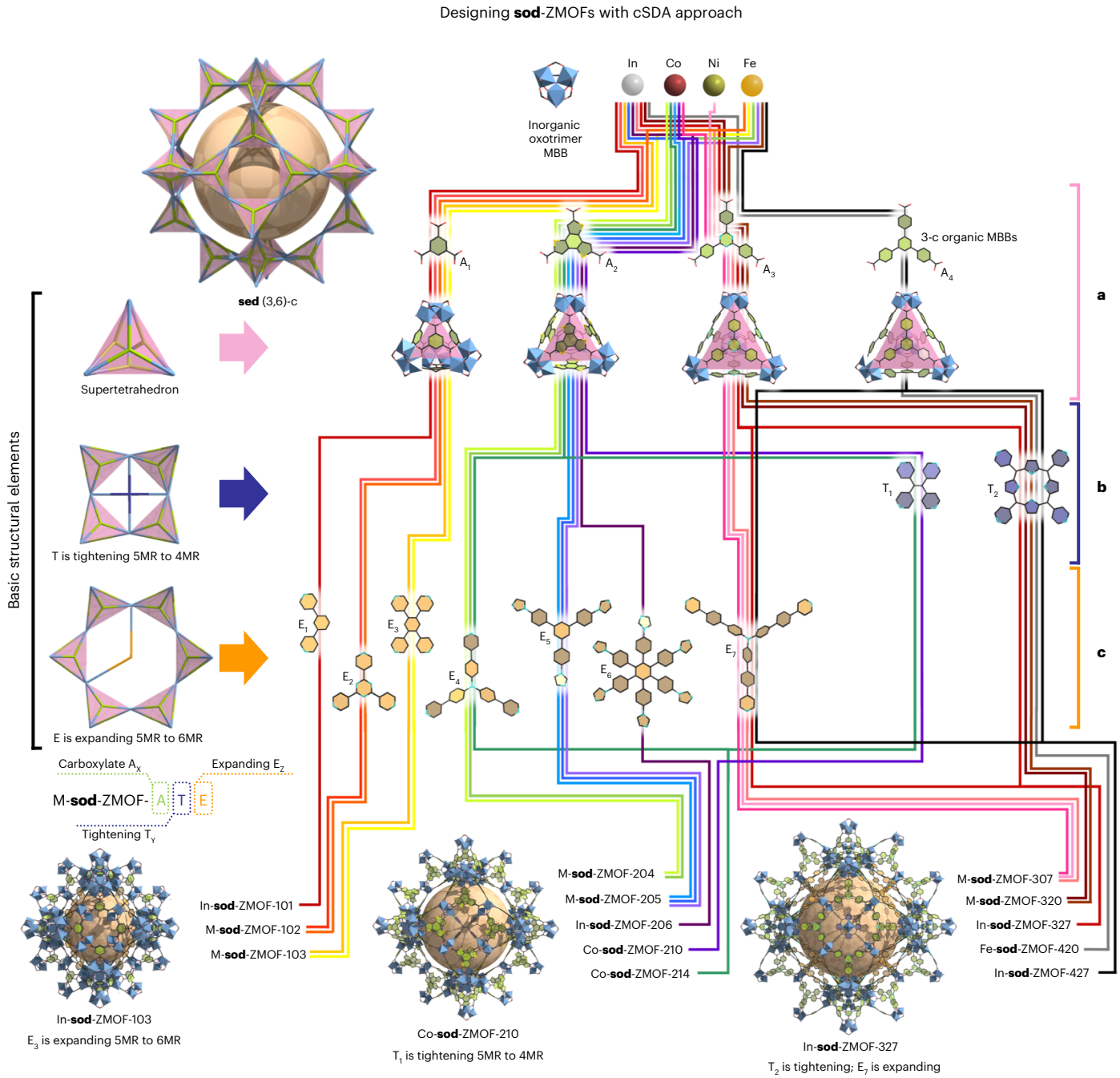

Fig. 1 | Design strategy to obtain ST-based ZMOFs with sodalite underlying topology by using cSDAs. a, Four types of STs constructed from inorganic oxotrimers $\{M_3O\}$ as tetrahedra vertices and tritopic carboxylate anions (**A**) as tetrahedra faces. **b**, Tightening-cSDA (**T**) to promote the square window (**4MR**). **c**, Expanding-cSDA (**E**) to promote the hexagonal window (**6MR**). Examples of three different **sod**-ZMOFs β-cages and 13 **sod**-ZMOF structural types obtained in this work.

sodalite windows was carried out. The arm length of tightening- and expanding-cSDAs (L_T and L_E, respectively) can be expressed as a function of the tritopic carboxylate ligand (L_A) forming the STs, by applying trigonometry rules (Fig. 3a)[41]. Accordingly, the following relations are obtained (Supplementary Fig. 9):

$$L_T = \sqrt{1.5}L_A - 0.9\text{Å}$$

$$L_E = \sqrt{3}L_A + 0.3\text{Å}$$

Suchwise, simple geometrical relations allow to express a rational dependence between the size of any equilateral tricarboxylate linker and corresponding N-ligands to fit either in square or hexagonal windows to promote the **sod** topology versus **mtn** in the formation of ST-based ZMOFs (Fig. 3b).

Design and synthesis of sod-ZMOFs with TATB or BTB ligands

By checking the size of accessible tricarboxylate ligands and possible tritopic cSDAs, a pair of ligands was predicted to precisely match the equation for **sod** net with expanding-cSDA (Fig. 3b) and consequently

https://doi.org/10.1038/s44160-023-00401-8

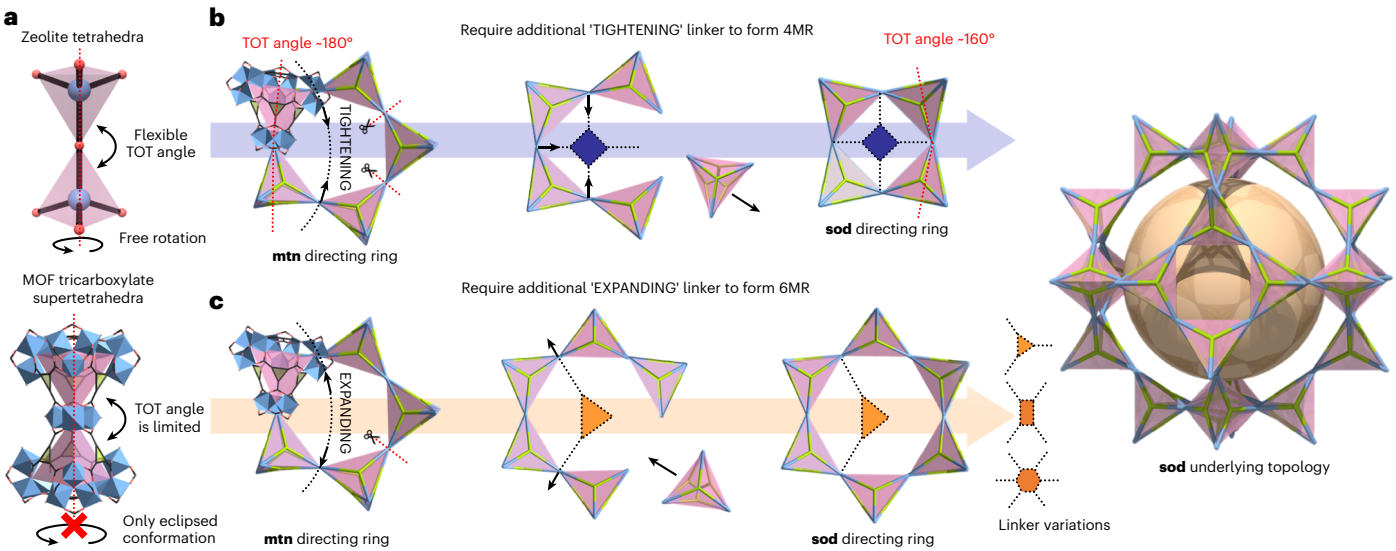

Fig. 2 | cSDA assembly concept. a, Relations between tetrahedra organization in zeolites and STs organization in ZMOFs. Schematic presentation of two possible ways to deviate from default **mtn** topology 5MR. **b**, Tightening apexes of neighbouring STs with polytopic cSDA decreasing TOT angle from 180° default for mtn topology to 160° for **sod** topology forming 4MR. **c**, Expanding two apexes of neighbouring STs with polytopic cSDA to form 6MR preventing 5MR formation.

allowed us to deliberately target and synthesize the corresponding **sod**-ZMOF (Fig. 4a).

Thus, In-**sod**-ZMOF-307 was synthesized solvothermally by heating indium salt with 2,4,6-tris(4-carboxyphenyl)-1,3,5-triazine (H_3TATB, $\mathbf{A_3}$), tris(4′-(pyridin-4-yl)-[1,1′-biphenyl]-4-yl)amine (PYB, $\mathbf{E_7}$) in appropriate conditions to ensure the in situ formation of the desired In trimers (Methods), yielding yellow rhombic dodecahedral single crystals of In-**sod**-ZMOF-307 (Supplementary Fig. 11j). Using Co or Ni salt gives brown and yellow rhombic dodecahedral single crystals of Co-**sod**-ZMOF-307 (Supplementary Fig. 11h) and Ni-**sod**-ZMOF-307 (Supplementary Fig. 11i), respectively.

Single-crystal X-ray diffraction (SCXRD) study revealed that all M-**sod**-ZMOF-307 crystallize in the *I*-43*m* space group with the unit cell parameters of 56.942(1), 56.6012(6) and 56.4345(8) Å, respectively, for In-**sod**-ZMOF-307, Co-**sod**-ZMOF-307, $(Et_2NH_2)_2[Co_3(\mu_3\text{-}O)(H_2O)_{1.83}(PYB)_{0.39}(TATB)_2]\cdot x$(guest) and Ni-**sod**-ZMOF-307, $(Et_2NH_2)_2[Ni_3(\mu_3\text{-}O)(H_2O)_{2.46}(PYB)_{0.18}(TATB)_2]\cdot x$(guest), where Et is CH_3CH_2 group. In-**sod**-ZMOF-307 was formulated as $[In_3(\mu_3\text{-}O)(H_2O)_{0.4}Br_{0.6}(PYB)_{2/3}(TATB)_2]Br_{0.4}\cdot x$(guest), which was confirmed by elemental analysis, proton nuclear magnetic resonance (^{1}H NMR) (Supplementary Fig. 36) and thermogravimetric analysis (TGA) (Supplementary Fig. 52). Phase purity of In-**sod**-ZMOF-307 was confirmed by powder X-ray diffraction (PXRD, Supplementary Fig. 25).

Structural analysis confirmed that the assembly of oxotrimers with TATB results in similar STs as in PCN-333 (ref. 32), but with an underlying **sod** topology. All adjacent STs are eclipsed from one another, connected through a shared oxotrimer. Hexagonal windows composed of six STs are capped by two PYB ligands, which act as the expanding-cSDAs, promoting the anticipated assembly into the **sod** topology (Fig. 2b). The experimental TOT angle was found to be 162°, in excellent agreement with the theoretical value (161°), while the TTT angle has been successfully increased to 120°, compatible with the hexagonal window.

From a topological point of view, the backbone of the structure, considering the supertetrahedral SBBs as nodes, exhibits the **sod** topology. The use of tritopic carboxylates to form the tetrahedra is well reflected by the recently predicted **sed** net resulting from face decoration of the edge net **sod-e** (ref. 42). However, in addition to 6 carboxylates, the connectivity of the oxotrimer is completed by two PYB ligands, making this trimer an 8-c MBB. The underlying topology, considering the contribution of the expanding-cSDAs is an unprecedented **sts** 3,3,8-c topology (**sts** stands for **sod**–super tetrahedra staggered capping) (Supplementary Fig. 76). The use of TATB as 3-c ligand yields big sizes of the STs and β-cages reaching 17 Å and 42 Å, respectively (the distance between two oxotrimers for ST and the shortest distance between opposite tetrahedra edges considering VdW radii for β-cage) (Supplementary Fig. 71). The β-cages are accessible through wide square windows of 16 Å and triangle ones of 10 Å between two cSDAs in 6MR (Supplementary Fig. 74).

Considering the successful assembly of **sod**-ZMOF, using expanding-cSDA to prevent the formation of pentagonal windows at the benefit of hexagonal ones, the strategy was further applied to the promotion of square windows (Fig. 2a). To that end, two additional ligand/cSDA couples were selected, fitting the second size dependency equation (Fig. 3b). Since 1,3,5-tris(4-carboxyphenyl)benzene (H_3BTB, $\mathbf{A_4}$) and H_3TATB are of comparable size, the 5,10,15,20-tetra(4-pyridyl)-21*H*,23*H*-porphine (TPPH, $\mathbf{T_2}$) was found to match both of them (Fig. 3b) and was used to demonstrates its possible use as tightening-cSDA to assemble **sod**-ZMOFs.

Solvothermal reaction of In or Fe salt in presence of H_3TATB and TPPH in conditions suitable to ensure the in situ formation of the desired In or Fe trimers yielded pink cubic single crystals of In-**sod**-ZMOF-320 (Supplementary Fig. 11k) and dark-greenish brown polycrystalline powder of Fe-**sod**-ZMOF-320. The use of H_3BTB instead of H_3TATB yielded dark-greenish brown polycrystalline powder of Fe-**sod**-ZMOF-420. SCXRD studies revealed that In-**sod**-ZMOF-320 crystallized in the cubic space group *Im*-3*m* with the unit cell parameter a = 57.312(3) Å. The compound was formulated as $[In_3(\mu_3\text{-}O)(H_2O)_2(TATB)_2(TPPH\text{-}In_{0.5}Br_{0.5})_{1/4}]Br\cdot x$(guest), which was also confirmed by elemental analysis, ^{1}H NMR (Supplementary Fig. 37) and TGA (Supplementary Fig. 54). The phase purity of the In-**sod**-ZMOF-320, Fe-**sod**-ZMOF-320, $[Fe_3(\mu_3\text{-}O)(H_2O)_2(TATB)_2(TPPH\text{-}Fe)_{1/4}]\cdot x$(guest), and Fe-**sod**-ZMOF-420, $[Fe_3(\mu_3\text{-}O)(H_2O)_2(BTB)_2(TPPH\text{-}Fe)_{1/4}]\cdot x$(guest), was confirmed by PXRD (Supplementary Figs. 26, 27 and 29).

From a topology point of view, the backbone of STs made with TATB and In oxotrimers, In-**sod**-ZMOF-320, follows once again the imposed **sod** topology. However, reflecting the expectation concerning the variation of the type of cSDA, the tightening-cSDA is located on

https://doi.org/10.1038/s44160-023-00401-8

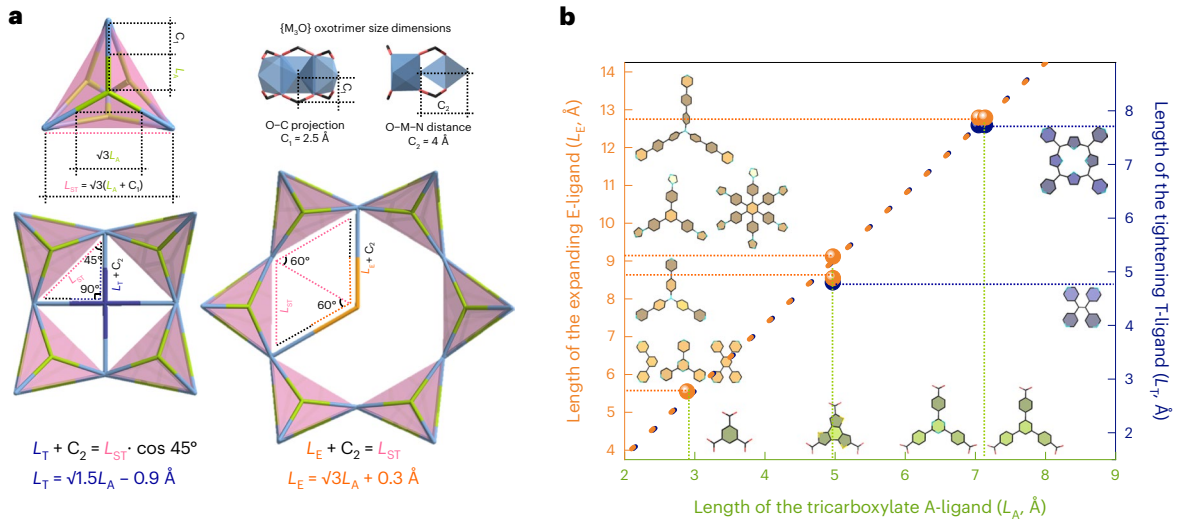

Fig. 3 | Geometry relations between sizes of ligands. a, Simplified representation of ST, 4MR and 6MR; oxotrimer size dimensions; calculated equations showing the relation between lengths of tightening-cSDA (L_T) or expanding-cSDA (L_E) and the length of tricarboxylate (L_A). **b**, Map showing the close matches around the calculated equations for expanding-cSDA (orange) and tightening-cSDA (dark blue).

the square window, where it plays its expected role and contributes to the formation of 4-c window, with TTT angle reduced from 108° (pentagon) to of 90° (square) (Fig. 2a). The connectivity and location of this cSDA has a direct impact on the formal topology of In-**sod**-ZMOF-320, leading to an unprecedented **stf** (3,4,7)-c net topology (**stf** stands for **sod**–super tetrahedra–four MR windows capped) (Supplementary Fig. 76). The size of the ST remains unaltered, 17 Å, but with β-cages of larger diameter of ca. 48 Å (Supplementary Fig. 71). The β-cages of obtained frameworks are accessible through wide hexagonal window of 26 Å diameter (Supplementary Fig. 74). These metrics directly place In-**sod**-ZMOF-320, Fe-**sod**-ZMOF-320 and Fe-**sod**-ZMOF-420 as the biggest sodalite related materials made so far, with β-cages diameter surpassing by ca. 12% the ones in the recently reported Zr-**sod**-ZMOF-1 (ca. 43 Å) (ref. 26).

Encouraged by the successful design and synthesis of In-**sod**-ZMOF-307 and In-**sod**-ZMOF-320, we found compelling to direct the rational synthesis of an additional **sod**-ZMOF, this time designed to have both hexagonal and square windows capped by the two types of cSDA, as the metrics of the three ligands are compatible with the equations. This is also possible structurally, due to the distinct and therefore compatible, binding location of the two types of cSDA on a single oxotrimer. Use of In salt with both PYB and TPPH as expanding- and tightening-cSDAs, respectively, yielded red cubic single crystals of In-**sod**-ZMOF-327 (Supplementary Fig. 11l) and red-brown rhombic dodecahedral single crystals of In-**sod**-ZMOF-427 (Supplementary Fig. 11m) using TATB and BTB ligands, respectively. SCXRD studies revealed that both compounds In-**sod**-ZMOF-327 and In-**sod**-ZMOF-427 crystallized in the cubic space group *I*-43*m* with the unit cell parameter *a* of 57.364(1) and 57.8453(8) Å, respectively. Compounds were formulated as $[In_3(\mu_3\text{-}O)(PYB)_{2/3}(TATB)_2(TPPH\text{-}In_{0.2}Br_{0.2})_{¼}]Br{\cdot}x(guest)$ and $[In_3(\mu_3\text{-}O)(BTB)_2(PYB)_{2/3}(TPPH\text{-}In_{0.26}Br_{0.26})_{¼}]Br{\cdot}x(guest)$, which was also confirmed by elemental analysis, ^{1}H NMR (Supplementary Figs. 38 and 39) and TGA (Supplementary Figs. 55 and 57). The phase purity of the In-**sod**-ZMOF-327 and In-**sod**-ZMOF-427 was confirmed by PXRD (Supplementary Figs. 28 and 30).

Besides the **sod** topology of the STs and considering the increased connectivity of the MBBs, the unprecedented **sfs** 3,3,4,9-c topology (**sfs** stands for **sod**–four & staggered capping) was observed (Supplementary Fig. 76). The β-cages of obtained framework (42 Å, Supplementary Fig. 71) are accessible through triangular windows of 6MR (10 Å) and rhombic windows of 4MR (9 Å) (Supplementary Fig. 74).

The presence of cSDA was computationally demonstrated to be critical for the stabilization of the **sod** net (Supplementary Fig. 126). The estimated difference between the energies of **mtn** and **sod** nets with the same composition (In and TATB-based ST) is 18.25 kcal mol^{-1} per ST unit, in favour of the **mtn** net. The calculated energies for In-**sod**-ZMOF-307 (8 PYB per unit cell), In-**sod**-ZMOF-320 (6 TPPH per unit cell) and In-**sod**-ZMOF-327 (8 PYB and 6 TPPH per unit cell) are −920, −1,560 and −477 kcal mol^{-1} per ST unit, respectively. This energy difference for In-**sod**-ZMOF-327 is most probably associated with the inherent flexibility of the PYB versus TPPH cSDAs, the geometry-optimized confined structure of this latter molecule being 0.2 Å shorter compared with its bulk geometry.

Design and synthesis of sod-ZMOFs with BTTC ligand

To validate the strength of our design approach, we embarked in synthesizing isoreticular **sod**-ZMOFs with other ligand/cSDA pairs (Fig. 3b). The next couples matching the equation for **sod** net with expanding-cSDA are benzo[1,2-b:3,4-b′:5,6-b″]trithiophene-2,5,8-tricarboxylic acid (H_3BTTC, $\mathbf{A_2}$) and tris(4-(pyridin-4-yl)phenyl)amine (PYM, $\mathbf{E_4}$).

The combination of H_3BTTC and PYM with Co or Fe salts in solvothermal conditions suitable to ensure the in situ formation of the desired Co or Fe trimers yielded red rhombic dodecahedral single crystals of Co-**sod**-ZMOF-204 (Supplementary Fig. 11c) and brown cubic crystals of Fe-**sod**-ZMOF-204 (Supplementary Fig. 11d), respectively. SCXRD studies revealed that both Co-**sod**-ZMOF-204 and Fe-**sod**-ZMOF-204 crystallized in the cubic space group *I*-43*m* with the unit cell parameter *a* of 44.876(1) and 44.6247(5) Å, respectively. Co-**sod**-ZMOF-204 and Fe-**sod**-ZMOF-204 were formulated as $(Et_2NH_2)_2[Co_3(\mu_3\text{-}O)(H_2O)_2(BTTC)_2(PYM)_{1/3}]{\cdot}x(guest)$ and $[Fe_3(\mu_3\text{-}O)(H_2O)_2(BTTC)_2(PYM)_{1/3}]{\cdot}x(guest)$, respectively, as confirmed by elemental analysis, X-ray photoelectron spectroscopy (XPS) (Supplementary Figs. 60 and 61) and TGA (Supplementary Figs. 45 and 46). The phase purity of both Co- and Fe-**sod**-ZMOF-204 was confirmed by PXRD (Supplementary Figs. 17 and 18).

The structural analysis confirmed the overall isoreticular nature of M-**sod**-ZMOF-204 with M-**sod**-ZMOF-307, where the BTTC connects the oxotrimers into STs. The tetrahedra are of 12.5 Å in size, while β-cages are 33 Å wide (Supplementary Fig. 69), accessible through the 10 Å square windows or through 12 Å windows defined by the hexagonal tetrahedra edge and two neighbouring pyridines (Supplementary Fig. 73).

https://doi.org/10.1038/s44160-023-00401-8

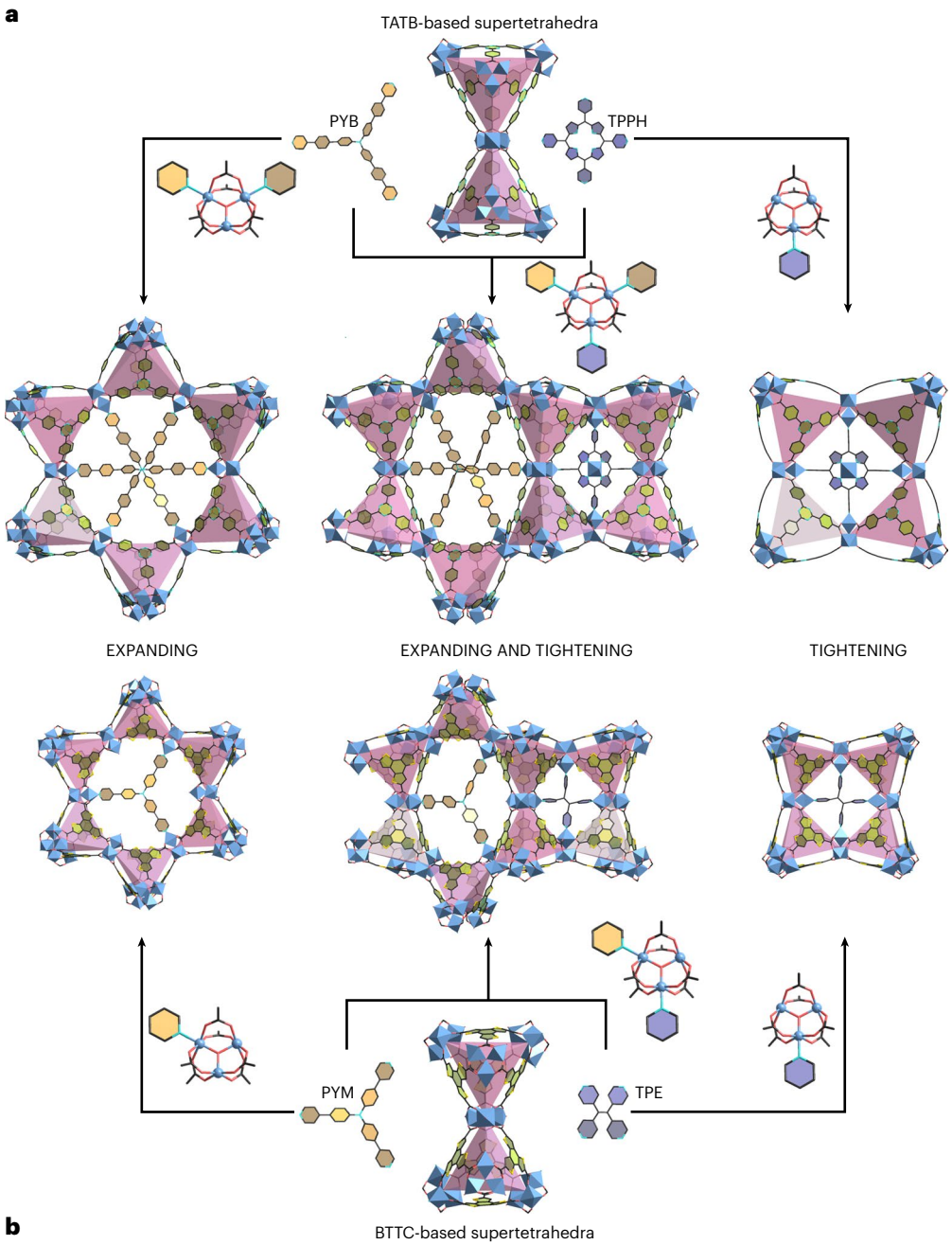

Fig. 4 | Implementation of 'EXPANDING' and 'TIGHTENING' strategies for sod-ZMOF design. a, TATB-based STs can be organized into 4MR using TPPH tightening-cSDA; into 6MR using 2 PYB expanding-cSDAs; into both 4MR and 6MR using both tightening- and expanding-cSDAs together. **b**, BTTC-based STs can be organized into 4MR using TPE tightening-cSDA; into 6MR using PYM expanding-cSDA; into both 4MR and 6MR using both tightening- and expanding-cSDAs together. Points at which pyridil coordinates to metal ion are specified in each case.

Same as with TATB- and BTB-based framework, not only expanding-cSDA can be used to obtain BTTC-based **sod**-ZMOFs, but also tightening-cSDA, or their combination. According to calculated dependency (Fig. 3b), there is one suitable tightening-cSDA, 1,1,2,2-tetra(pyridin-4-yl)ethene (TPE, $\mathbf{T_1}$). The combination of H_3BTTC with Co salt and TPE in solvothermal conditions yielded yellow cubic crystals of Co-**sod**-ZMOF-210 (Supplementary Fig. 11f). SCXRD studies revealed that Co-**sod**-ZMOF-210 crystallized in the cubic space group *I*432 with the unit cell parameter a = 44.7093(5) Å. Compound was formulated as $(Et_2NH_2)_2[Co_3(\mu_3\text{-}O)(H_2O)_2(BTTC)_2(TPE)_{1/4}]\cdot x$(guest) as confirmed by elemental analysis, XPS (Supplementary Fig. 63) and TGA (Supplementary Fig. 50). The phase purity of Co-**sod**-ZMOF-210 was confirmed by PXRD (Supplementary Fig. 23). β-Cages are 37 Å wide (Supplementary Fig. 69), accessible through the 20-Å-wide hexagonal windows (Supplementary Fig. 73).

The use of both types of cSDA, PYM and TPE, in one synthesis with BTTC yielded brown rhombic dodecahedral crystals in case of Co (Supplementary Fig. 11g) giving Co-**sod**-ZMOF-214. SCXRD studies revealed that Co-**sod**-ZMOF-214 crystallized in the cubic space group *I*-43*m* with the unit cell parameter a = 44.7671(6) Å. Compound was formulated as $(Et_2NH_2)_2[Co_3(\mu_3\text{-}O)(H_2O)(BTTC)_2(PYM)_{1/3}(TPE)_{1/4}]\cdot x$ (guest) as confirmed by elemental analysis, XPS (Supplementary Fig. 64) and TGA (Supplementary Fig. 51). The phase purity of Co-**sod**-ZMOF-214 was confirmed by PXRD (Supplementary Fig. 24).

β-Cages are 33 Å wide (Supplementary Fig. 69), accessible through 12 Å windows between the hexagonal tetrahedra edge and two neighbouring pyridines, and small trigonal 4 Å windows between two neighbouring pyridines in 4MR (Supplementary Fig. 73).

While the examples presented above successfully validated of the strength of the design and synthesis approach, we aimed to demonstrate that, with the richness of organic chemistry, additional pairs of ligands can match the equations and yield additional **sod**-ZMOFs.

The combination of BTTC ligand, 1,1′-(5′-(4-(1*H*-imidazol-1-yl) phenyl)-[1,1′:3′,1′′-terphenyl]-4,4′′-diyl)bis(1*H*-imidazole) (IMI, $\mathbf{E_5}$) (Fig. 3b) with Co, Fe or In salts in solvothermal conditions yielded pink cubic single crystals of Co-**sod**-ZMOF-205 (Supplementary Fig. 11e), brown microcrystalline powder of Fe-**sod**-ZMOF-205 and colourless microcrystalline powder of In-**sod**-ZMOF-205, respectively. SCXRD studies revealed that Co-**sod**-ZMOF-205 crystallized in the cubic space group *I*-43*m* with the unit cell parameter $a = 45.130(3)$ Å. The compounds were formulated as $(Et_2NH_2)_2[Co_3(\mu_3\text{-}O)(H_2O)_{5/3}(BTTC)_2(IMI)_{2/3}]\cdot x$(guest), $[Fe_3(\mu_3\text{-}O)(H_2O)_{5/3}(BTTC)_2(IMI)_{2/3}]\cdot x$(guest) and $[In_3(\mu_3\text{-}O)Br(BTTC)_2(IMI)_{2/3}]\cdot x$(guest) confirmed by elemental analysis, XPS (Supplementary Fig. 62), ^{1}H NMR (Supplementary Fig. 34) and TGA (Supplementary Figs. 47–49). The phase purity of Co-, Fe- and In-**sod**-ZMOF-205 was confirmed by PXRD (Supplementary Figs. 19–21).

The overall structure of Co-**sod**-ZMOF-205 is similar to Co-**sod**-ZMOF-204, with underlying **sod** topology. However, a noticeable difference with Co-**sod**-ZMOF-204 was observed: due to steric hindrance, the IMI tightening-cSDA is not planar, and only two of its three arms are coordinated (Supplementary Fig. 73). Thus, there are two 2-c IMI molecules per hexagonal window in Co-**sod**-ZMOF-205 with their third arm pointing towards the inside of the β-cage (Supplementary Fig. 69). Thus, β-cage size ranges from 12 Å to 37 Å (Supplementary Fig. 70). In this case, IMI acts as ditopic bend ligand with angle of 120° that is enough to direct formation of **sod**-ZMOF instead of **mtn**-ZMOF.

As it is possible to have two staggered tritopic *cSDAs* occupying one 6MR window, it is expected that a single hexatopic ligand could direct the structure in a similar way. The combination of H_3BTTC and 1,2,3,4,5,6-hexakis(4-(1*H*-imidazol-1-yl)phenyl)benzene (IM6, $\mathbf{E_6}$) with In salt in solvothermal conditions yielded colourless microcrystalline powder of In-**sod**-ZMOF-206. The compound was formulated as $[In_3(\mu_3\text{-}O)Br(BTTC)_2(IM6)_{1/3}]\cdot 1/3(IM6)\cdot x$(guest), as confirmed by elemental analysis, ^{1}H NMR (Supplementary Fig. 35), PXRD (Supplementary Fig. 22) and TGA (Supplementary Fig. 49).

Design and synthesis of sod-ZMOFs with BTC

To expand our approach over boundaries we selected more various examples of ligand/cSDA pairs. We reasoned that a bent ligand, 1,3-di(pyridin-4-yl)benzene (IDPB, $\mathbf{E_1}$) ligand, offering two pyridine rings with 120° angle between them should be sufficient to expand two opposite apexes of adjacent STs to promote 6MR instead of 5MR (Fig. 2b and Supplementary Fig. 72). The combination of benzene-1,3,5-tricarboxylic acid (H_3BTC, $\mathbf{A_1}$) and IDPB with In salt in solvothermal conditions yielded colourless microcrystalline powder of In-**sod**-ZMOF-101. The compound was formulated as $[In_3(\mu_3\text{-}O)(H_2O)(BTC)_2Cl_{2/3}(IDPB)_{2/3}]Cl_{1/3}\cdot x$(guest), as confirmed by elemental analysis, ^{1}H NMR (Supplementary Fig. 31), PXRD (Supplementary Fig. 12) and TGA (Supplementary Fig. 40).

The next couple matching the equation for **sod** net with expanding-cSDA is H_3BTC and 2,4,6-tri(4-pyridyl)-1,3,5-triazine (TPT, $\mathbf{E_2}$) (Fig. 3b). In-**sod**-ZMOF-102 and Fe-**sod**-ZMOF-102 were synthesized by heating solvothermally the corresponding metal salt with H_3BTC, TPT in appropriate conditions for the in situ formation of the desired In or Fe trimers (see Methods), yielding colourless octahedron crystals of In-**sod**-ZMOF-102 (Supplementary Fig. 11a) and light-brown microcrystalline powder of Fe-**sod**-ZMOF-102, respectively.

SCXRD studies revealed that In-**sod**-ZMOF-102 crystallizes in the *Im*-3*m* space group with the unit cell parameter $a = 33.7480(5)$ Å. The compound was formulated as $[In_3(\mu_3\text{-}O)(H_2O)(BTC)_2(TPT)_{1/3}]Cl\cdot 0.5(H_2O)\cdot x$(guest), as confirmed by elemental analysis, ^{1}H NMR (Supplementary Fig. 32) and TGA (Supplementary Fig. 41). Phase purity of both In- and Fe-**sod**-ZMOF-102, $[Fe_3(\mu_3\text{-}O)(H_2O)_2(BTC)_2(TPT)_{1/3}]\cdot x$(guest), was confirmed by PXRD (Supplementary Figs. 13 and 14).

The resulting In-**sod**-ZMOF-102 has two types of cavities; small tetrahedra of ca. 9.5 Å are formed by four oxotrimers as vertices and four BTC linkers as faces. The second cavity corresponds to the β-cage of the sodalite net with diameter of 24 Å (Supplementary Fig. 68). The β-cage has six square windows, and eight hexagonal windows capped with TPT. The hexagonal windows appear to be fully blocked with TPT and coordinated anion, while the square windows have a small 3 Å aperture that could be increased to 6 Å upon dehydration/desolvation (Supplementary Fig. 72). The symmetry unambiguously allows distinguishing one ordered TPT cSDA per hexagonal window while other three open metal sites in the same window are occupied by halogen anions. In contrast, Fe-**sod**-ZMOF-102 does not contain any halogen anions due to mixed Fe^{2+}/Fe^{3+} composition in oxotrimer, as confirmed by XPS (Supplementary Fig. 58) and elemental analysis. In these cases, the formal topology differs from the one of In-**sod**-ZMOF-307 due to lower connectivity of In trimers.

Since a single cSDA is sufficient to expand two opposite apexes of adjacent STs and deviate from 5MR to 6MR, we designed and synthesized related ZMOFs using this time less intuitive, rectangular cSDA of appropriate size, expected to bind four of the six oxotrimers located at the vertices of the hexagonal windows. Adding 1,2,4,5-tetra(pyridin-4-yl)benzene (TPB, $\mathbf{E_3}$) ligand to the corresponding mixtures of In or Fe salts and H_3BTC in appropriate conditions yielded colourless rhombic dodecahedral crystals of In-**sod**-ZMOF-103 (Supplementary Fig. 11b) and light-brown microcrystalline powder of Fe-**sod**-ZMOF-103. SCXRD studies revealed that In-**sod**-ZMOF-103 crystallizes in the cubic space group *Im*-3*m* with the unit cell parameter $a = 33.880(1)$ Å. The compound was formulated as $[In_3(\mu_3\text{-}O)(H_2O)_{0.93}Br_{0.74}(BTC)_2(TPB)_{1/3}]Br_{0.26}\cdot 0.5(H_2O)\cdot x$(guest) further confirmed by elemental analysis, ^{1}H NMR (Supplementary Fig. 33) and TGA (Supplementary Fig. 43). Phase purity of both In- and Fe-**sod**-ZMOF-103, $[Fe_3(\mu_3\text{-}O)(H_2O)_{5/3}(BTC)_2(TPB)_{1/3}]\cdot x$(guest), was confirmed by PXRD (Supplementary Figs. 15 and 16).

The TPB cSDA of In-**sod**-ZMOF-103 acts similarly as the TPT ligand capping the 6MR and disordered over three equal positions. The hexagonal windows are fully blocked by TPB ligand and coordinated bromide anions (Supplementary Figs. 68 and 72). In this case, the formal topology differs from the one of In-**sod**-ZMOF-102.

Overall, such on-demand tuning possibilities of the pore dimensions, access windows and metal cation show potential for this versatile **sod**-ZMOF platform to produce separating agents with small pore aperture, while also allowing, by the formation of colossal mesopores in the bigger analogues, highly porous materials to be developed to address gas storage needs (Fig. 5a).

Low-pressure gas sorption studies

The permanent porosity of obtained materials was established by measuring Ar sorption at 87 K and N_2 at 77 K (Fig. 5c and Supplementary Figs. 77–109). In-**sod**-ZMOF-307, In-**sod**-ZMOF-320, In-**sod**-ZMOF-327, Fe-**sod**-ZMOF-320 and Fe-**sod**-ZMOF-420 showed reversible isotherms characteristic for mesoporous materials with one type of cavity (Supplementary Figs. 103–107). TPPH-based In-**sod**-ZMOF-320, Fe-**sod**-ZMOF-320 and Fe-**sod**-ZMOF-420 also have a slightly visible hysteresis between adsorption and desorption traces. Obtained characteristic sorption values are in a good agreement with calculated ones (Supplementary Table 16). Experimental total pore volume of 3.15 $cm^3\,g^{-1}$ for Fe-**sod**-ZMOF-420 is in a good agreement with calculated values of 3.40 $cm^3\,g^{-1}$, and the highest reported value among any sodalite related

https://doi.org/10.1038/s44160-023-00401-8

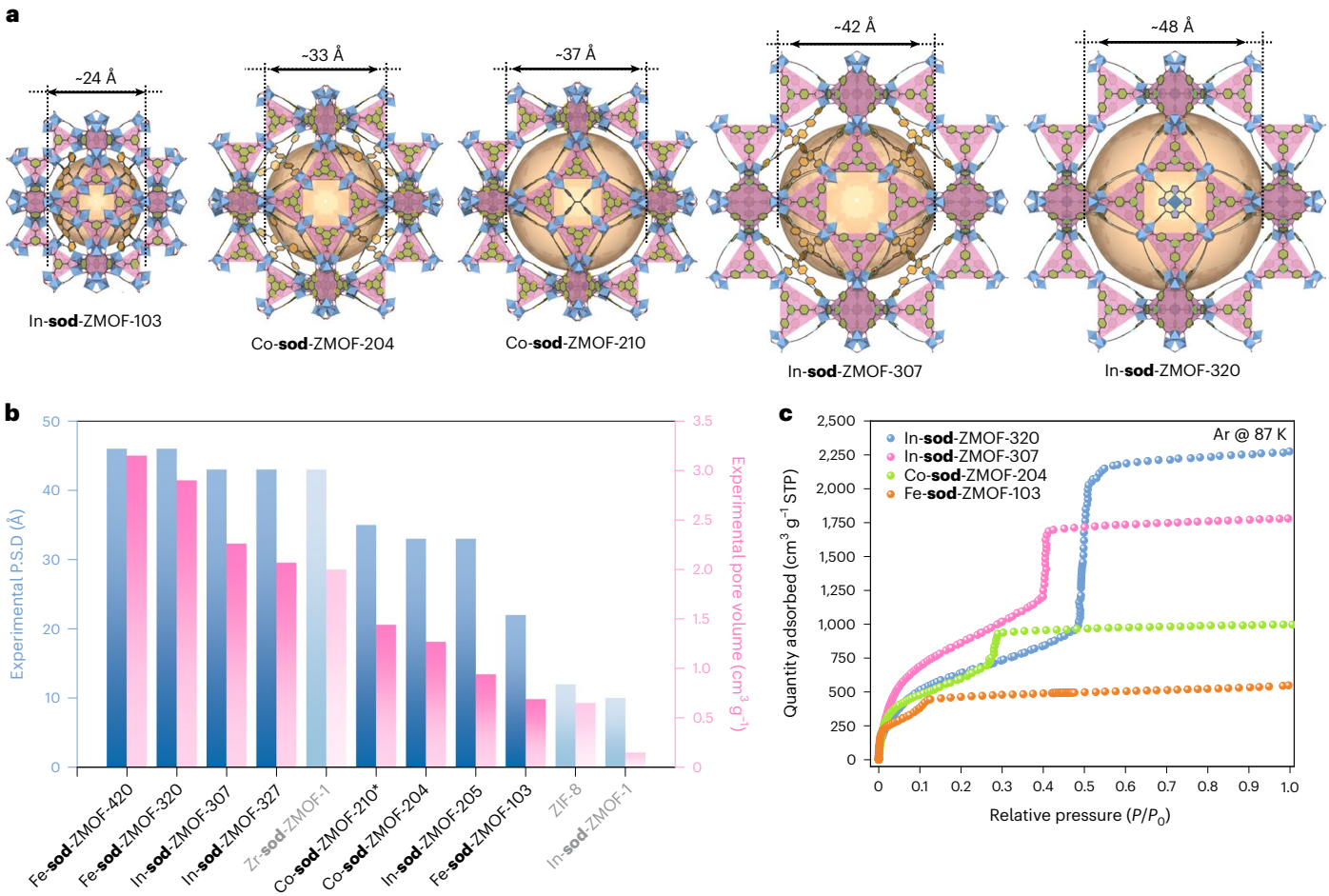

Fig. 5 | Comparison of cage sizes and adsorption properties of different structure types of obtained MOF. a, Range of **sod**-ZMOF β-cages. For BTC-ST ZMOF cage is shown with expanding-cSDA (TPB); for BTTC-ST ZMOFs two types of cages with expanding (PYM) and tightening (TPE) cSDAs are presented; for TATB-ST ZMOFs two types of cages with expanding (PYB) and tightening (TPPH) cSDAs are presented. Estimated from SCXRD data, sizes of β-cages in angstroms are marked above. **b**, Comparison between **sod**-ZMOFs reported in the paper and other **sod**-ZMOFs (shown in pale). Experimental total pore volumes calculated from Ar 87 K sorption isotherms are shown with pink rectangles; pore size distribution (PSD) average size for each ZMOF calculated from Ar 87 K sorption isotherms shown with blue rectangles; asterisk indicates pore volume is calculated from N_2 77 K sorption isotherm. **c**, Ar 87 K sorption isotherms for different **sod**-ZMOFs demonstrating increasing of sorption capacity with mesoporous sorption region shift (STP, standard temperature and pressure).

material (Fig. 5b)[23,26,43]. Experimental total pore volumes of In-**sod**-ZMOFs materials are 2.89, 2.26 and 2.07 $cm^3 g^{-1}$ for In-**sod**-ZMOF-320, In-**sod**-ZMOF-307 and In-**sod**-ZMOF-327, respectively, and predictably decreasing with inclusion of additional organic moieties. The corresponding series of BTTC-based frameworks Co-**sod**-ZMOF-210, Co-**sod**-ZMOF-204 and Co-**sod**-ZMOF-214 has close total pore volume values giving 1.06, 1.27 and 1.18 $cm^3 g^{-1}$, respectively. The pore size distribution (PSD) for In-**sod**-ZMOF-3TE and Co-**sod**-ZMOF-2TE series (Supplementary Figs. 110–118) was assessed using the Ar adsorption data (Supplementary Figs. 98, 101–104 and 106) and revealed two types of pore for In-**sod**-ZMOF-3T7 and Co-**sod**-ZMOF-204 series with mesopore sizes of 43 Å and 33 Å, respectively, which are in good qualitative agreement with the above derived values of 42 Å and 33 Å from the corresponding calculated structure.

Co-**sod**-ZMOF-205 has a lower expected total pore volume than the isoreticular In-**sod**-ZMOF due to its anionic framework, which requires the presence of counterions inside the cavities, and ligand arms pointing inside the cavities (Supplementary Figs. 99 and 100). The total pore volume of Co-**sod**-ZMOF-205 is 0.65 $cm^3 g^{-1}$. In-**sod**-ZMOF-205 demonstrates high Ar uptake with total pore volume of 0.94 $cm^3 g^{-1}$ (calculated 1.09 $cm^3 g^{-1}$). The PSD for In-**sod**-ZMOF-205 was assessed using the Ar adsorption data (Supplementary Fig. 100) and revealed two types of pore, with mesopore size of 33 Å, in perfect qualitative agreement with the above-derived values from the corresponding calculated structure.

Fe-**sod**-ZMOF-102 has a total pore volume of 0.80 $cm^3 g^{-1}$ (Supplementary Fig. 96). This experimental value is close to the calculated one (0.87 $cm^3 g^{-1}$). The PSD for Fe-**sod**-ZMOF-102 was assessed using the Ar adsorption data and revealed one type of pore with diameter of 24 Å, which is in good qualitative agreement with the above-derived value from the corresponding calculated structure. Fe-**sod**-ZMOF-103 has expectedly lower total pore volume of 0.69 $cm^3 g^{-1}$ than Fe-**sod**-ZMOF-102 due to the additional pyridine ring in the ligand structure (Supplementary Fig. 97). Among series of In-**sod**-ZMOF-10E only In-**sod**-ZMOF-101 showed adsorption capacity of 0.62 $cm^3 g^{-1}$ comparable with the calculated value of 0.58 $cm^3 g^{-1}$ (Supplementary Fig. 77) due to fully blocked entrances to inner cavities with coordinated anions and water molecules in other analogues.

High-pressure gas sorption and storage studies

Reduction of greenhouse gas emissions as well as the search for alternative fuel vectors/sources are priority areas of modern energy. The use of methane as a fuel makes it possible to reduce the amount of harmful emissions of carbon monoxide and dioxide, primarily due to

https://doi.org/10.1038/s44160-023-00401-8

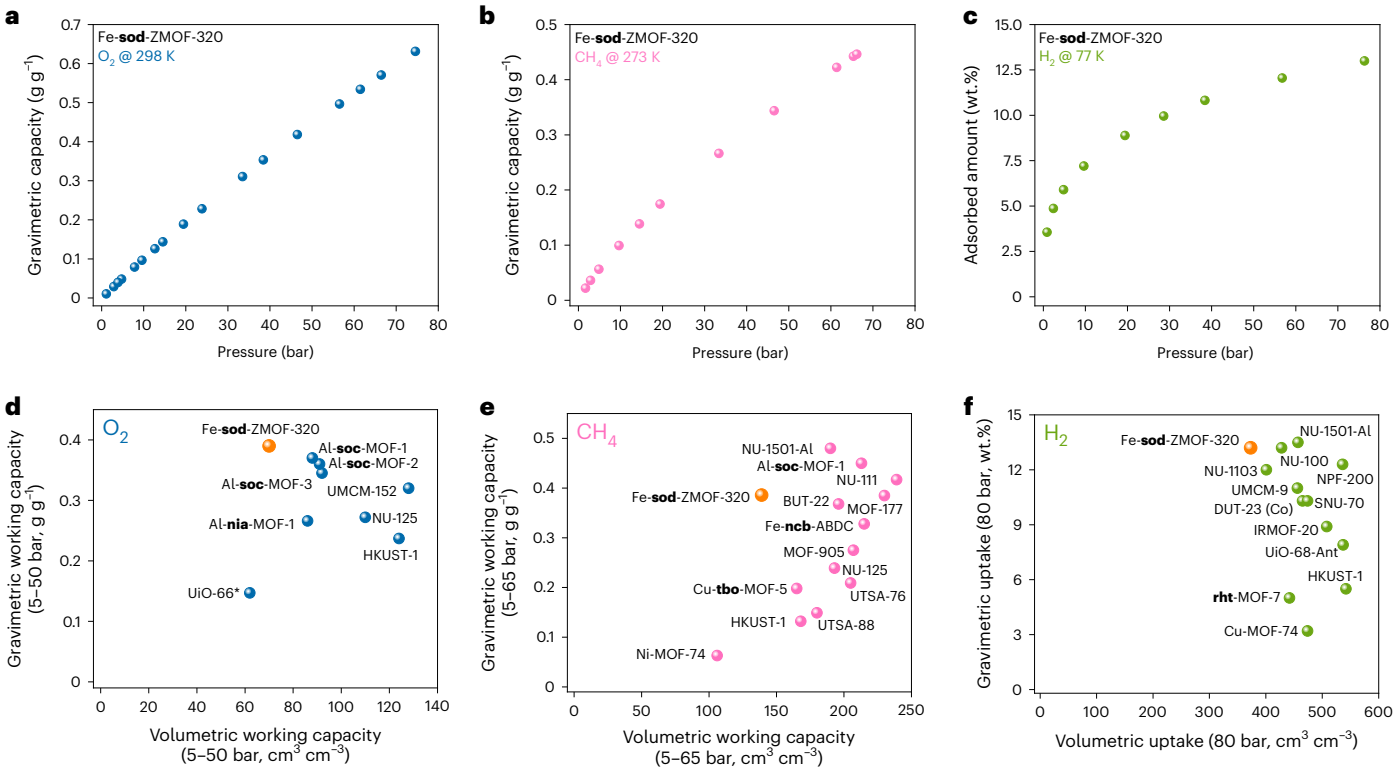

Fig. 6 | Adsorption properties of selected materials. a–**c**, Oxygen at 298 K (**a**), methane at 273 K (**b**) and hydrogen at 77 K (**c**) sorption isotherms on Fe-**sod**-ZMOF-320. **d**,**e**, Working capacities of 5–50 bar O_2 for Fe-**sod**-ZMOF-320 in comparison with the best MOF materials for O_2 storage at 298 K (**d**), and 5–65 bar CH_4 working capacities for Fe-**sod**-ZMOF-320 in comparison with the best MOF materials for CH_4 storage at 273 K (**e**). **f**, H_2 gravimetric and volumetric uptakes for Fe-**sod**-ZMOF-320 in comparison with the best MOF materials for H_2 storage at 77 K, up to 80 bar. Asterisk indicates the UiO-66 value was obtained from O_2 isotherm collected up to 30 bar, extrapolated to 50 bar.

the highest ratio of H to C compared with any other hydrocarbons[44,45]. An alternative to methane is traditionally hydrogen, which, in turn, is completely freed from carbon monoxide and carbon dioxide emissions during combustion and meets the requirements of green energy in its native measure[46]. Thus, it is vital to develop sorbents that allow such gases to be stored and used as efficiently as possible within an acceptable range of temperatures and pressures.

While this area of application has already received wide attention from researchers, the storage of other gases at high pressure is still much less studied and developed. In particular, there are categorically few examples of MOFs for oxygen storage[47], critical in many key applications pertaining to medical and aerospace industries. The recent coronavirus pandemic has highlighted the importance of improving oxygen storage conditions, for safety reasons, with the aim to increase the amount of stored oxygen while keeping the pressure moderate.

The proposed strategy of expanding and tightening cSDAs made it possible to obtain a wide range of isoreticular compounds in which the pore volume can be varied both by changing the length of the tricarboxylate ligand and by varying the appropriate cSDA. In addition, using both T and E alone, or in combination, allows us to vary the surface area in the same parent **sed** substructure. Compounds with the highest pore volume values are best suited for studying their gas storage ability at high pressure. Due to their high accessible and total pore volumes and the presence of open metal sites, BTB- and TATB-based **sod**-ZMOFs should be regarded as most promising candidates. Accordingly, O_2, H_2 and CH_4 sorption experiments were conducted at variable temperatures, up to 80 bar on Fe-**sod**-ZMOF-320, the most promising example due to its high experimental N_2 pore volume (3.21 $cm^3\ g^{-1}$) to carry out all high-pressure measurements (Fig. 6).

The guest free Fe-**sod**-ZMOF-320 sample was subjected to high-pressure gas sorption measurements to assess the associated storage capacity at different temperatures. Figure 6a,d shows oxygen gravimetric adsorption isotherm at 298 K and comparison of gravimetric working capacities of reported MOFs at 298 K 5–50 bar. Obtained value of 0.39 g g^{-1} for Fe-**sod**-ZMOF-320 sets a benchmark for any MOF material so far outperforming such compounds as Al-**soc**-MOF series[48], UMCM-152 (ref. 49) and NU-125 (ref. 50). Such a high capacity makes Fe-**sod**-ZMOF-320 an ideal potential adsorbent for oxygen storage. A substantial increase in capacity allows for a cylinder at high pressure to store more oxygen, therefore requiring less frequent recharging, ultimately reducing the cost of oxygen storage, or even allowing for smaller cylinders for easier transport.

Efficient sorbents for methane storage should offer adequate balance between gravimetric and volumetric capacities, and the corresponding US Department of Energy targets (350 $cm^3\ cm^{-3}$ and 0.5 g g^{-1}, respectively) remain an ongoing challenge. It has been proposed that a slight reduction of the storage temperature to nearly 273 K could improve both the volumetric and gravimetric uptake[51]. Methane sorption isotherm measured at 273 K (Fig. 6b) revealed very high gravimetric uptake, placing it among the best MOF materials, such as NU-1501 (ref. 52), Al-**soc**-MOF-1 (ref. 48) and NU-111 (ref. 53). Gravimetric uptake for Fe-**sod**-ZMOF-320 at 273 K and 65 bar reaches 0.44 g g^{-1}, a value that is anticipated to exceed the US Department of Energy target at relatively higher but still acceptable pressures. The volumetric capacity for Fe-**sod**-ZMOF-320 at 273 K and 65 bar reaches 156 $cm^3\ cm^{-3}$, relatively lower than the best values achieved for Al-**soc**-MOF-1 (ref. 48), MOF-177 (ref. 54) or NU-111 (ref. 53). A comprehensive comparison of absolute methane uptakes and working capacities for our Fe-**sod**-ZMOF-320 with the best reported MOF materials so far

under different temperature and pressure conditions is presented in Fig. 6e and Supplementary Table 17. Fe-**sod**-ZMOF-320 displayed very high gravimetric and considerable volumetric working capacities at different working temperatures and pressures. This notable feature is a result of the reduced unused CH_4 uptake below 5 bar and the linear trend of the CH_4 isotherms at relatively high pressures. Considering this promising sorption assessment, we believe that the demonstrated high modularity of this **sod**-ZMOF platform will permit, by appropriate combination of metal ion, tricarboxylate ligand and one or two cSDAs, a precise control over the structures and further improvement of the volumetric/gravimetric working capacity balance.

Due to its extremely high total pore volume, Fe-**sod**-ZMOF-320 shows very high H_2 uptake reaching 13 wt% (Fig. 6c) at 76 bar and 77 K, which is comparable with benchmark reported MOFs NU-1501-Al (ref. 52), NU-100 (ref. 55) and NPF-200 (ref. 56) under similar conditions. A comprehensive comparison of gravimetric and volumetric capacities for our Fe-**sod**-ZMOF-320 with the best reported MOF materials so far is presented in Fig. 6e and Supplementary Table 18.

Conclusions and outlook

Throughout this work, we have designed, synthesized and characterized a family of more than twenty isoreticular materials within the **sod**-ZMOFs platform. The use of centring SDAs ensured the promotion of the **sod** backbone over any other tetrahedral nets (diamond, quartz, other zeolitic nets and so on), yet allowing for a wide porosity diversity, both on the pore accessibility (pore aperture) and volume (cavity size). This diversity is reflected by the possibility to target made-to-order MOFs with contracted pore aperture suitable for various key separations, but also with high pore volumes, reflected by experimental oxygen, methane and hydrogen sorption capacities of Fe-**sod**-ZMOF-320, with gravimetric uptakes surpassing those of most of the best sorbent materials so far.

Moreover, the multinary nature of these ZMOFs, with multiple components ordered in crystallographically distinct positions, capping either the square, the hexagonal or both window types suggests possibilities for the observation of multiple interaction mechanisms located on distinct sites, with tunable distances and sequences.

Finally, we envision this tightening/expanding cSDA strategy will enable possibilities for the design and synthesis of meaningful materials, taking advantage of the large variety of readily available inorganic MBBs and 'polymorph-compatible' topologies.

Methods

All reagents were obtained from commercial sources and used without further purification (unless otherwise noted in 'Organic synthesis' section in Supplementary Information). No metal salt nor ligand stock solutions were prepared.

Synthesis of In-sod-ZMOF-101

$InCl_3$ (22.1 mg, 0.100 mmol), H_3BTC (13.9 mg, 0.067 mmol), IDPB (5.1 mg, 0.022 mmol), HBF_4 (0.4 ml), methanol (2.0 ml) and *N*,*N*-diethylformamide (DEF) (4.0 ml) were combined in a 20 ml scintillation vial, which was then sonicated for 30 min, placed in pre-heated oven at 115 °C for 24 h, and cooled to room temperature. The colourless microcrystalline powder was collected by centrifugation and washed with *N*,*N*-dimethylformamide (DMF). Crystals were soaked in DMF overnight, and then exchanged in methanol for 3 days and dried in oven at 85 °C. Note that the methanol solution was refreshed at least twice a day. Elemental analysis found (calculated) for $C_{28.67}ClH_{20}In_3N_{1.33}O_{16}$: C% 33.78 (33.79), H% 1.98 (1.98), N% 2.03 (1.83). The yield is 50%, based on metal.

Synthesis of In-sod-ZMOF-102

$InCl_3$ (22.1 mg, 0.100 mmol), H_3BTC (13.9 mg, 0.067 mmol), TPT (3.4 mg, 0.011 mmol), HBF_4 (0.3 ml) and DEF (5.0 ml) were combined in a 34 ml Pyrex vial, which was then sonicated for 30 min, placed in pre-heated oven at 150 °C for 24 h, and cooled to room temperature. The colourless octahedron crystals were collected by centrifugation and washed with DMF. Crystals were soaked in DMF overnight, and then exchanged in methanol for 3 days and dried in oven at 85 °C. Note that the methanol solution was refreshed at least twice a day. Elemental analysis found (calculated) for $C_{24}ClH_{14}In_3N_2O_{15}$: C% 31.47 (30.33), H% 1.43 (1.48), N% 2.39 (2.95). The yield is 71%, based on metal.

Synthesis of Fe-sod-ZMOF-102

$FeCl_3{\cdot}6H_2O$ (60.8 mg, 0.225 mmol), H_3BTC (31.5 mg, 0.150 mmol), TPT (15.6 mg, 0.050 mmol), HBF_4 (0.2 ml), DEF (5.0 ml) and methanol (1.0 ml) were combined in a 20 ml scintillation vial, which was then sonicated for 30 min, placed in pre-heated oven at 105 °C for 24 h, and cooled to room temperature. The light-brown microcrystalline powder was collected by centrifugation and washed with DMF. Crystals were soaked in DMF overnight, and then exchanged in methanol for 3 days and dried in oven at 85 °C. Note that the methanol solution was refreshed at least twice a day. Elemental analysis found (calculated) for $C_{24}Fe_3H_{18}N_2O_{17}$: C% 37.70 (37.25), H% 2.55 (2.34), N% 3.42 (3.62). The yield is 77%, based on metal.

Synthesis of In-sod-ZMOF-103

$InBr_3$ (35.5 mg, 0.100 mmol), H_3BTC (13.9 mg, 0.067 mmol), TPB (4.2 mg, 0.011 mmol), HBF_4 (0.3 ml) and DEF (5.0 ml) were combined in a 34 ml Pyrex vial, which was then sonicated for 30 min, placed in pre-heated oven at 150 °C for 24 h, and cooled to room temperature. The colourless rhombic dodecahedral crystals were collected by centrifugation and washed with DMF. Crystals were soaked in DMF overnight, and then exchanged in methanol for 3 days and dried in oven at 85 °C. Note that the methanol solution was refreshed at least twice a day. Elemental analysis found (calculated) for $BrC_{26.67}H_{16}In_3N_{1.33}O_{15}$: C% 30.95 (31.42), H% 1.57 (1.58), N% 1.88 (1.83). The yield is 47%, based on metal.

Synthesis of Fe-sod-ZMOF-103

$FeCl_3{\cdot}6H_2O$ (60.8 mg, 0.225 mmol), H_3BTC (31.5 mg, 0.150 mmol), TPB (8.8 mg, 0.025 mmol), HBF_4 (0.2 ml), DEF (5.0 ml) and methanol (1.0 ml) were combined in a 20 ml scintillation vial, which was then sonicated for 30 min, placed in pre-heated oven at 105 °C for 24 h, and cooled to room temperature. The light-brown microcrystalline powder was collected by centrifugation and washed with DMF. Crystals were soaked in DMF overnight, and then exchanged in methanol for 3 days and dried in oven at 85 °C. Note that the methanol solution was refreshed at least twice a day. Elemental analysis found (calculated) for $C_{26.67}Fe_3H_{22}N_{1.33}O_{18}$: C% 39.63 (39.22), H% 2.68 (2.72), N% 2.28 (2.29). The yield is 58%, based on metal.

Synthesis of Co-sod-ZMOF-204

$CoCl_2{\cdot}6H_2O$ (23.8 mg, 0.100 mmol), H_3BTTC (25.2 mg, 0.067 mmol), PYM (5.2 mg, 0.011 mmol), trifluoroacetic acid (TFA) (0.3 ml) and DEF (5.0 ml) were combined in a 34 ml Pyrex vial, which was then sonicated for 30 min, placed in pre-heated oven at 150 °C for 24 h, and cooled to room temperature. The red rhombic dodecahedral crystals were collected by centrifugation and washed with DMF. Crystals were soaked in DMF overnight, and then exchanged in ethanol and then hexane for 3 days and dried in oven at 85 °C. Note that the methanol solution was refreshed at least twice a day. Elemental analysis found (calculated) for $C_{49}Co_3H_{48}N_{3.33}O_{18}S_6$: C% 42.95 (43.89), H% 3.34 (3.61), N% 3.38 (3.48), S% 14.58 (14.35). The yield is 63%, based on metal.

Synthesis of Fe-sod-ZMOF-204

$FeCl_2{\cdot}4H_2O$ (22.0 mg, 0.100 mmol), H_3BTTC (25.2 mg, 0.066 mmol), PYM (5.2 mg, 0.011 mmol), TFA (0.3 ml) and DEF (5.0 ml) were combined in a 34 ml Pyrex vial, which was then sonicated for 30 min, placed in pre-heated oven at 150 °C for 24 h, and cooled to room temperature.

The brown cubic crystals were collected by centrifugation and washed with DMF. Crystals were soaked in DMF overnight, and then exchanged in ethanol and then hexane for 3 days and dried in oven at 85 °C. Note that the methanol solution was refreshed at least twice a day. Elemental analysis found (calculated) for $C_{41}Fe_3H_{28}N_{1.33}O_{20}S_6$: C% 39.66 (40.39), H% 2.33 (2.31), N% 1.56 (1.53), S% 15.36 (15.78). The yield is 53%, based on metal.

Synthesis of Co-sod-ZMOF-205

$CoCl_2{\cdot}6H_2O$ (11.9 mg, 0.050 mmol), H_3BTTC (12.6 mg, 0.033 mmol), IMI (5.6 mg, 0.011 mmol), TFA (0.3 ml) and DEF (5.0 ml) were combined in a 34 ml Pyrex vial, which was then sonicated for 30 min, placed in pre-heated oven at 150 °C for 24 h, and cooled to room temperature. The pink cubic crystals were collected by centrifugation and washed with DMF. Crystals were soaked in DMF overnight, and then exchanged in methanol for 3 days and dried in oven at 85 °C. Note that the methanol solution was refreshed at least twice a day. Elemental analysis found (calculated) for $C_{60}Co_3H_{52}N_6O_{16}S_6$: C% 49.26 (48.62), H% 3.58 (3.54), N% 5.39 (5.67), S% 12.34 (12.98). The yield is 15%, based on metal.

Synthesis of Fe-sod-ZMOF-205

$FeCl_3$ (60.8 mg, 0.225 mmol), H_3BTTC (28.5 mg, 0.075 mmol), IMI (19.0 mg, 0.038 mmol), HBF_4 (1.0 ml) and DEF (25.0 ml) were combined in a 70 ml Pyrex vial, which was then sonicated for 30 min, placed in pre-heated oven at 150 °C for 24 h, and cooled to room temperature. The brown microcrystalline powder was collected by centrifugation and washed with DMF. The yield is 22%, based on H_3BTTC.

Synthesis of In-sod-ZMOF-205

$InBr_3$ (79.8 mg, 0.225 mmol), H_3BTTC (28.5 mg, 0.075 mmol), IMI (19.0 mg, 0.038 mmol), HBF_4 (1.0 ml) and DEF (25.0 ml) were combined in a 70 ml Pyrex vial, which was then sonicated for 30 min, placed in pre-heated oven at 150 °C for 24 h, and cooled to room temperature. The colourless microcrystalline powder was collected by centrifugation and washed with DMF. Crystals were soaked in DMF overnight, and then exchanged in methanol for 3 days and dried in oven at 85 °C. Note that the methanol solution was refreshed at least twice a day. Elemental analysis found (calculated) for $BrC_{52}H_{40}In_3N_4O_{22}S_6$: C% 35.81 (36.96), H% 1.95 (2.39), N% 3.28 (3.32), S% 11.42 (11.39). The yield is 28%, based on H_3BTTC.

Synthesis of In-sod-ZMOF-206

$InBr_3$ (79.8 mg, 0.225 mmol), H_3BTTC (28.5 mg, 0.075 mmol), IM6 (19.0 mg, 0.019 mmol), HBF_4 (1.0 ml) and DEF (25.0 ml) were combined in a 70 ml Pyrex vial, which was then sonicated for 30 min, placed in pre-heated oven at 150 °C for 24 h, and cooled to room temperature. The colourless microcrystalline powder was collected by centrifugation and washed with DMF. Crystals were soaked in DMF overnight, and then exchanged in methanol for 3 days and dried in oven at 85 °C. Note that the methanol solution was refreshed at least twice a day. Elemental analysis for $BrC_{70}H_{40}In_3N_8O_{16}S_6$: C% 44.92 (45.06), H% 2.62 (2.16), N% 5.56 (6.01), S% 10.50 (10.31). The yield is 10%, based on H_3BTTC.

Synthesis of Co-sod-ZMOF-210

$CoCl_2{\cdot}6H_2O$ (23.8 mg, 0.100 mmol), H_3BTTC (25.2 mg, 0.0676 mmol), TPE (3.7 mg, 0.011 mmol), TFA (0.3 ml) and DEF (5.0 ml) were combined in a 34 ml Pyrex vial, which was then sonicated for 30 min, placed in pre-heated oven at 150 °C for 24 h, and cooled to room temperature. The yellow rhombic dodecahedral crystals were collected by centrifugation and washed with DMF. Crystals were soaked in DMF overnight, and then exchanged in ethanol and then hexane for 3 days and dried in oven at 85 °C. Note that the methanol solution was refreshed at least twice a day. Elemental analysis found (calculated) for $C_{43.5}Co_3H_{40}N_3O_{16}S_6$: C% 41.11 (42.48), H% 2.42 (3.28), N% 3.69 (3.42), S% 15.47 (15.64). The yield is 45%, based on metal.

Synthesis of Co-sod-ZMOF-214

$CoCl_2{\cdot}6H_2O$ (23.8 mg, 0.100 mmol), H_3BTTC (25.2 mg, 0.067 mmol), PYM (5.2 mg, 0.011 mmol), TPE (3.7 mg, 0.011 mmol), TFA (0.3 ml) and DEF (5.0 ml) were combined in a 34 ml Pyrex vial, which was then sonicated for 30 min, placed in pre-heated oven at 150 °C for 24 h, and cooled to room temperature. The brown rhombic dodecahedral crystals were collected by centrifugation and washed with DMF. Crystals were soaked in DMF overnight, and then exchanged in ethanol and then hexane for 3 days and dried in oven at 85 °C. Note that the methanol solution was refreshed at least twice a day. Elemental analysis found (calculated) for $C_{54.5}Co_3H_{48}N_{4.33}O_{16}S_6$: C% 46.54 (47.13), H% 2.96 (3.48), N% 4.90 (4.37), S% 14.02 (13.85). The yield is 45%, based on metal.

Synthesis of Co-sod-ZMOF-307

$CoCl_2{\cdot}6H_2O$ (23.8 mg, 0.100 mmol), H_3TATB (14.6 mg, 0.033 mmol), PYB (7.8 mg, 0.011 mmol), TFA (0.3 ml) and DEF (5.0 ml) were combined in a 70 ml Pyrex vial, which was then sonicated for 30 min, placed in pre-heated oven at 150 °C for 24 h, and cooled to room temperature. The brown rhombic dodecahedral crystals were collected by centrifugation and washed with DMF.

Synthesis of Ni-sod-ZMOF-307

$NiCl_2{\cdot}6H_2O$ (23.8 mg, 0.100 mmol), H_3TATB (14.6 mg, 0.033 mmol), PYB (7.8 mg, 0.011 mmol), TFA (0.3 ml) and DEF (5.0 ml) were combined in a 70 ml Pyrex vial, which was then sonicated for 30 min, placed in pre-heated oven at 150 °C for 24 h. The yellow rhombic dodecahedral crystals were collected by centrifugation and washed with DMF.

Synthesis of In-sod-ZMOF-307

$InBr_3$ (35.5 mg, 0.100 mmol), H_3TATB (14.6 mg, 0.033 mmol), PYB (7.8 mg, 0.011 mmol), HBF_4 (0.3 ml), DEF (5.0 ml) and methanol (1.0 ml) were combined in a 70 ml Pyrex vial, which was then sonicated for 30 min, placed in pre-heated oven at 85 °C for 24 h, and cooled to room temperature. The yellow rhombic dodecahedral crystals were collected by centrifugation and washed with DMF. Crystals were soaked in DMF/dichloromethane (DCM) overnight, and then exchanged in ethanol for 3 days and then in hexane for 1 day and dried in oven at 85 °C. Note that the ethanol and hexane solution was refreshed at least twice a day. Elemental analysis found (calculated) for $BrC_{82}H_{60}In_3N_{8.67}O_{19}$: C% 51.23 (51.97), H% 3.11 (3.19), N% 6.54 (6.41). The yield is 56%, based on H_3TATB.

Synthesis of In-sod-ZMOF-320

$InBr_3$ (35.5 mg, 0.100 mmol), H_3TATB (14.6 mg, 0.033 mmol), TPPH (3.4 mg, 0.006 mmol), HBF_4 (0.3 ml), DEF (5.0 ml) and methanol (1.0 mL) were combined in a 70 ml Pyrex vial, which was then sonicated for 30 min, placed in pre-heated oven at 85 °C for 24 h, and cooled to room temperature. The pink cubic crystals were collected by centrifugation and washed with DMF. Crystals were soaked in DMF/DCM overnight, and then exchanged in ethanol for 3 days and then in hexane for 1 day and dried in oven at 85 °C. Note that the ethanol and hexane solution was refreshed at least twice a day. Elemental analysis found (calculated) for $Br_{1.25}C_{58}H_{38}In_{3.25}N_8O_{17}$: C% 44.23 (43.76), H% 2.91 (2.41), N% 6.95 (7.04). The yield is 40%, based on H_3TATB.

Synthesis of Fe-sod-ZMOF-320

$FeCl_3{\cdot}6H_2O$ (27.0 mg, 0.100 mmol), H_3TATB (14.6 mg, 0.033 mmol), TPPH (6.8 mg, 0.011 mmol), TFA (0.3 ml), DCM (5.0 ml), methanol (5.0 ml) and DEF (2.0 ml) were combined in a 70 ml Pyrex vial, which was then sonicated for 30 min, placed in pre-heated oven at 85 °C for 24 h, and cooled to room temperature. The greenish brown microcrystalline powder was collected by centrifugation and washed with DMF. Crystals were soaked in DMF/DCM overnight, and then exchanged in ethanol for 3 days and then in hexane for 1 day and dried in oven at 85 °C. Note that the ethanol and hexane solution was refreshed at least twice a day.

Elemental analysis found (calculated) for $C_{58}Fe_{3.25}H_{42}N_8O_{19}$: C% 52.46 (52.12), H% 2.62 (3.17), N% 7.68 (8.38). The yield is 65%, based on H_3TATB.

Synthesis of In-sod-ZMOF-327

$InBr_3$ (35.5 mg, 0.100 mmol), H_3TATB (14.6 mg, 0.033 mmol), PYB (7.8 mg, 0.011 mmol), TPPH (3.4 mg, 0.006 mmol), HBF_4 (0.3 ml), DEF (5.0 ml) and methanol (1.0 ml) were combined in a 70 ml Pyrex vial, which was then sonicated for 30 min, placed in pre-heated oven at 85 °C for 24 h, and cooled to room temperature. The red cubic crystals were collected by centrifugation and washed with DMF. Crystals were soaked in DMF/DCM overnight, and then exchanged in ethanol for 3 days and then in hexane for 1 day and dried in oven at 85 °C. Note that the ethanol and hexane solution was refreshed at least twice a day. Elemental analysis for $Br_{1.25}C_{92}H_{65}In_{3.25}N_{10.67}O_{18}$: C% 53.43 (53.10), H% 3.21 (3.15), N% 7.14 (7.18). The yield is 62%, based on H_3TATB.

Synthesis of Fe-sod-ZMOF-420

$FeCl_3{\cdot}6H_2O$ (27.0 mg, 0.100 mmol), H_3BTB (14.5 mg, 0.033 mmol), TPPH (6.8 mg, 0.011 mmol), TFA (0.3 ml), DCM (5.0 ml), methanol (5.0 ml) and DEF (2.0 ml) were combined in a 70 ml Pyrex vial, which was then sonicated for 30 min, placed in pre-heated oven at 85 °C for 24 h, and cooled to room temperature. The greenish brown microcrystalline powder was collected by centrifugation and washed with DMF. Crystals were soaked in DMF/DCM overnight, and then exchanged in ethanol for 3 days and then in hexane for 1 day and dried in oven at 85 °C. Note that the ethanol and hexane solution was refreshed at least twice a day. Elemental analysis found (calculated) for $C_{64}Fe_{3.25}H_{46}N_2O_{18}$: C% 58.06 (58.56), H% 3.64 (3.53), N% 2.66 (2.13). The yield is 71%, based on H_3BTB.

Synthesis of In-sod-ZMOF-427

$InBr_3$ (35.5 mg, 0.100 mmol), H_3BTB (14.6 mg, 0.033 mmol), PYB (7.8 mg, 0.011 mmol), TPPH (3.4 mg, 0.006 mmol), HBF_4 (0.3 ml), DEF (5.0 ml) and methanol (1.0 ml) were combined in a 70 ml Pyrex vial, which was then sonicated for 30 min, placed in pre-heated oven at 85 °C for 24 h, and cooled to room temperature. The red-brown rhombic dodecahedral crystals were collected by centrifugation and washed with DMF. Crystals were soaked in DMF/DCM overnight, and then exchanged in ethanol for 3 days and then in hexane for 1 day and dried in oven at 85 °C. Note that the ethanol and hexane solution was refreshed at least twice a day. Elemental analysis found (calculated) for $Br_{1.25}C_{98}H_{70}In_{3.25}N_{4.67}O_{18}$: C% 56.21 (56.75), H% 3.37 (3.40), N% 3.80 (3.15). The yield is 63%, based on H_3BTB.

Note that similar reactions as the ones described above, with deliberate omission of cSDAs in the synthetic mixture do not yield, in any case, to **sod**-ZMOF formation. In most cases an **mtn**-ZMOF is formed.

Structures and compositions of the obtained compounds were confirmed by elemental analysis, ^{1}H NMR (Supplementary Fig. 31–39), TGA (Supplementary Figs. 40–57) and XPS (Supplementary Figs. 58–66). Phase purity was confirmed by PXRD (Supplementary Figs. 12–30).

Data availability

The X-ray crystallographic coordinates for structures reported in this study have been deposited at the Cambridge Crystallographic Data Centre (CCDC), under deposition numbers CCDC 2261737 (In-**sod**-ZMOF-102), 2261738 (In-**sod**-ZMOF-103), 2261739 (Co-**sod**-ZMOF-210), 2261740 (Co-**sod**-ZMOF-204), 2261741 (Fe-**sod**-ZMOF-204), 2261742 (Co-**sod**-ZMOF-205), 2261743 (Co-**sod**-ZMOF-214), 2261744 (In-**sod**-ZMOF-320), 2261745 (Co-**sod**-ZMOF-307), 2261746 (In-**sod**-ZMOF-307), 2261747 (Ni-**sod**-ZMOF-307), 2261748 (In-**sod**-ZMOF-327) and 2261749 (In-**sod**-ZMOF-427). These data can be obtained free of charge from The Cambridge Crystallographic Data Centre via www.ccdc.cam.ac.uk/data_request/cif.

References

1. Freund, R. et al. 25 years of reticular chemistry. *Angew. Chem. Int. Ed.* **60**, 23946–23974 (2021).
2. Moghadam, P. Z. et al. Development of a Cambridge Structural Database subset: a collection of metal–organic frameworks for past, present, and future. *Chem. Mater.* **29**, 2618–2625 (2017).
3. Guillerm, V. & Eddaoudi, M. The importance of highly connected building units in reticular chemistry: thoughtful design of metal–organic frameworks. *Acc. Chem. Res.* **54**, 3298–3312 (2021).
4. Chen, Z. et al. Reticular chemistry in the rational synthesis of functional zirconium cluster-based MOFs. *Coord. Chem. Rev.* **386**, 32–49 (2019).
5. Guillerm, V. et al. A supermolecular building approach for the design and construction of metal–organic frameworks. *Chem. Soc. Rev.* **43**, 6141–6172 (2014).
6. Eddaoudi, M., Sava, D. F., Eubank, J. F., Adil, K. & Guillerm, V. Zeolite-like metal–organic frameworks (ZMOFs): design, synthesis, and properties. *Chem. Soc. Rev.* **44**, 228–249 (2015).
7. Liu, X. & Liu, Y. Recent progress in the design and synthesis of zeolite-like metal–organic frameworks (ZMOFs). *Dalton Trans.* **50**, 3450–3458 (2021).
8. Horcajada, P. et al. Metal–organic frameworks as efficient materials for drug delivery. *Angew. Chem. Int. Ed.* **45**, 5974–5978 (2006).
9. Horcajada, P. et al. Porous metal–organic-framework nanoscale carriers as a potential platform for drug delivery and imaging. *Nat. Mater.* **9**, 172–178 (2010).
10. Hwang, Y. K. et al. Amine grafting on coordinatively unsaturated metal centers of MOFs: consequences for catalysis and metal encapsulation. *Angew. Chem. Int. Ed.* **47**, 4144–4148 (2008).
11. Alkordi, M. H., Liu, Y., Larsen, R. W., Eubank, J. F. & Eddaoudi, M. Zeolite-like metal–organic frameworks as platforms for applications: on metalloporphyrin-based catalysts. *J. Am. Chem. Soc.* **130**, 12639–12641 (2008).
12. Latroche, M. et al. Hydrogen storage in the giant-pore metal–organic frameworks MIL-100 and MIL-101. *Angew. Chem. Int. Ed.* **45**, 8227–8231 (2006).
13. Al-Maythalony, B. A. et al. Quest for anionic MOF membranes: continuous sod-ZMOF membrane with CO_2 adsorption-driven selectivity. *J. Am. Chem. Soc.* **137**, 1754–1757 (2015).
14. Mohideen, M. I. H. et al. Upgrading gasoline to high octane numbers using a zeolite-like metal-organic framework molecular sieve with ana-topology. *ChemComm* **54**, 9414–9417 (2018).
15. Pan, Y. & Lai, Z. Sharp sepaÿration of C2/C3 hydrocarbon mixtures by zeolitic imidazolate framework-8 (ZIF-8) membranes synthesized in aqueous solutions. *ChemComm* **47**, 10275–10277 (2011).
16. Yoon, J. W. et al. Selective nitrogen capture by porous hybrid materials containing accessible transition metal ion sites. *Nat. Mater.* **16**, 526–531 (2017).
17. O'Keeffe, M., Peskov, M. A., Ramsden, S. J. & Yaghi, O. M. The Reticular Chemistry Structure Resource (RCSR) database of, and symbols for, crystal nets. *Acc. Chem. Res.* **41**, 1782–1789 (2008).
18. The Reticular Chemistry Structure Resource. *RCSR* http://rcsr.anu.edu.au/. Accessed 20 Jan 2020
19. Database of zeolite structures. *Structure Commission of the International Zeolite Association* http://europe.iza-structure.org/IZA-SC/ftc_table.php. Accessed 20 Jan 2020
20. Pophale, R., Cheeseman, P. A. & Deem, M. W. A database of new zeolite-like materials. *Phys. Chem. Chem. Phys.* **13**, 12407–12412 (2011).
21. The Atlas of Prospective Zeolite Structures. *Hypothetical Zeolithes* http://www.hypotheticalzeolites.net/. Accessed 20 Jan 2020

22. Liu, Y., Kravtsov, V. & Eddaoudi, M. Template-directed assembly of zeolite-like metal–organic frameworks (ZMOFs): a usf-ZMOF with an unprecedented zeolite topology. *Angew. Chem. Int. Ed.* **47**, 8446–8449 (2008).
23. Liu, Y. L., Kravtsov, V. C., Larsen, R. & Eddaoudi, M. Molecular building blocks approach to the assembly of zeolite-like metal–organic frameworks (ZMOFs) with extra-large cavities. *Chem. Commun.* **2006**, 1488–1490 (2006).
24. Alkordi, M. H. et al. Zeolite-like metal–organic frameworks (ZMOFs) based on the directed assembly of finite metal–organic cubes (MOCs). *J. Am. Chem. Soc.* **131**, 17753–17755 (2009).
25. Sava, D. F. et al. Exceptional stability and high hydrogen uptake in hydrogen-bonded metal-organic cubes possessing ACO and AST zeolite-like topologies. *J. Am. Chem. Soc.* **131**, 10394–10395 (2009).
26. Alsadun, N. et al. Introducing a cantellation strategy for the design of mesoporous zeolite-like metal–organic frameworks: Zr-sod-ZMOFs as a case study. *J. Am. Chem. Soc.* **142**, 20547–20553 (2020).
27. Park, K. S. et al. Exceptional chemical and thermal stability of zeolitic imidazolate frameworks. *Proc. Natl Acad. Sci. USA* **103**, 10186–10191 (2006).
28. Banerjee, R. et al. High-throughput synthesis of zeolitic imidazolate frameworks and application to CO_2 capture. *Science* **319**, 939–943 (2008).
29. Ferey, G. et al. A hybrid solid with giant pores prepared by a combination of targeted chemistry, simulation, and powder diffraction. *Angew. Chem. Int. Ed.* **43**, 6296–6301 (2004).
30. Ferey, G. et al. A chromium terephthalate-based solid with unusually large pore volumes and surface area. *Science* **309**, 2040–2042 (2005).
31. O'Keeffe, M. Tetrahedral frameworks TX2 with T–X–T angle=180°: rationalization of the structures of MOF-500 and of MIL-100 and MIL-101. *Mater. Res. Bull.* **41**, 911–915 (2006).
32. Feng, D. et al. Stable metal-organic frameworks containing single-molecule traps for enzyme encapsulation. *Nat. Commun.* **6**, 5979 (2015).
33. Liu, Q. et al. Mesoporous cages in chemically robust MOFs created by a large number of vertices with reduced connectivity. *J. Am. Chem. Soc.* **141**, 488–496 (2019).
34. Wang, H. Z., Pei, X. K., Kalmutzki, M. J., Yang, J. J. & Yaghi, O. M. Large cages of zeolitic imidazolate frameworks. *Acc. Chem. Res.* **55**, 707–721 (2022).
35. Horcajada, P. et al. Extended and functionalized porous iron(iii) tri- or dicarboxylates with MIL-100/101 topologies. *ChemComm* **50**, 6872–6874 (2014).
36. Chevreau, H. et al. Mixed-linker hybrid superpolyhedra for the production of a series of large-pore iron(III) carboxylate metal–organic frameworks. *Angew. Chem. Int. Ed.* **52**, 5056–5060 (2013).
37. Virmani, E., Beyer, O., Lüning, U., Ruschewitz, U. & Wuttke, S. Topology-guided functional multiplicity of iron(iii)-based metal–organic frameworks. *Mater. Chem. Front.* **1**, 1965–1974 (2017).
38. Zhang, L. et al. A window-space-directed assembly strategy for the construction of supertetrahedron-based zeolitic mesoporous metal–organic frameworks with ultramicroporous apertures for selective gas adsorption. *Chem. Sci.* **12**, 5767–5773 (2021).
39. Guillerm, V. & Maspoch, D. Geometry mismatch and reticular chemistry: strategies to assemble metal–organic frameworks with non-default topologies. *J. Am. Chem. Soc.* **141**, 16517–16538 (2019).
40. Zhang, Y.-B., Zhang, W.-X., Feng, F.-Y., Zhang, J.-P. & Chen, X.-M. A highly connected porous coordination polymer with unusual channel structure and sorption properties. *Angew. Chem. Int. Ed.* **48**, 5287–5290 (2009).
41. Jiang, H. et al. Enriching the reticular chemistry repertoire: merged nets approach for the rational design of intricate mixed-linker metal–organic framework platforms. *J. Am. Chem. Soc.* **140**, 8858–8867 (2018).
42. Guillerm, V. & Eddaoudi, M. Material design and reticular chemistry: unveiling new topologies through face decoration of edge nets. *Ind. Eng. Chem. Res.* **61**, 12641–12648 (2022).
43. Sava, D. F. et al. Quest for zeolite-like metal-organic frameworks: on pyrimidinecarboxylate bis-chelating bridging ligands. *J. Am. Chem. Soc.* **130**, 3768–3770 (2008).
44. Lozano-Castello, D., Alcaniz-Monge, J., de la Casa-Lillo, M. A., Cazorla-Amoros, D. & Linares-Solano, A. Advances in the study of methane storage in porous carbonaceous materials. *Fuel* **81**, 1777–1803 (2002).
45. He, Y. B., Zhou, W., Qian, G. D. & Chen, B. L. Methane storage in metal–organic frameworks. *Chem. Soc. Rev.* **43**, 5657–5678 (2014).
46. Allendorf, M. D. et al. An assessment of strategies for the development of solid-state adsorbents for vehicular hydrogen storage. *Energ. Environ. Sci.* **11**, 2784–2812 (2018).
47. Sutton, A. L., Melag, L., Sadiq, M. M. & Hill, M. R. Capture, storage, and release of oxygen by metal–organic frameworks (MOFs). *Angew. Chem. Int. Ed.* **61**, e2022083 (2022).
48. Alezi, D. et al. MOF crystal chemistry paving the way to gas storage needs: aluminum-based soc-MOF for CH_4, O_2, and CO_2 storage. *J. Am. Chem. Soc.* **137**, 13308–13318 (2015).
49. Moghadam, P. Z. et al. Computer-aided discovery of a metal-organic framework with superior oxygen uptake. *Nat. Commun.* **9**, 1378 (2018).
50. DeCoste, J. B. et al. Metal–organic frameworks for oxygen storage. *Angew. Chem. Int. Ed.* **53**, 14092–14095 (2014).
51. Li, B., Wen, H. M., Zhou, W., Xu, J. Q. & Chen, B. L. Porous metal–organic frameworks: promising materials for methane storage. *Chem* **1**, 557–580 (2016).
52. Chen, Z. J. et al. Balancing volumetric and gravimetric uptake in highly porous materials for clean energy. *Science* **368**, 297–303 (2020).
53. Peng, Y. et al. Simultaneously high gravimetric and volumetric methane uptake characteristics of the metal-organic framework NU-111. *ChemComm* **49**, 2992–2994 (2013).
54. Furukawa, H. et al. Ultrahigh porosity in metal–organic frameworks. *Science* **329**, 424–428 (2010).
55. Ahmed, A. et al. Exceptional hydrogen storage achieved by screening nearly half a million metal–organic frameworks. *Nat. Commun.* **10**, 1568 (2019).
56. Zhang, X. et al. Optimization of the pore structures of MOFs for record high hydrogen volumetric working capacity. *Adv. Mater.* **32**, 1907995 (2020).

Acknowledgements

Research reported in this publication was supported by the King Abdullah University of Science and Technology (KAUST). S.R.G.B. was supported with Grant POSTDOC_21_00069 funded by Consejería de Transformación Económica, Industria, Conocimiento y Universidades and Agencia Andaluza del Conocimiento, Junta de Andalucía. We are thankful to C3UPO for the HPC facilities provided.

Author contributions

M.E. and V.G. formulated the project. A.C.S. and P.P. synthesized organic linkers. M. Bar. and A. Sap. synthesized and characterized the compounds. A. Shk. performed SCXRD analysis. A.A. and M. Bon. performed low-pressure sorption measurements. P.M.B. and M. Bon. performed high-pressure sorption measure. O.S. performed XPS analysis. S.R.G.B., R.S. and G.M. performed analysis of existing zeolitic topologies and molecular simulations of the ZMOFs. M.E., V.G., M. Bar. and A. Sap. wrote the paper, and all the authors contributed to revising it.

Competing interests
The authors declare no competing interests.

Additional information
Supplementary information The online version contains supplementary material available at https://doi.org/10.1038/s44160-023-00401-8.

Correspondence and requests for materials should be addressed to Vincent Guillerm or Mohamed Eddaoudi.

Peer review information *Nature Synthesis* thanks Banglin Chen, Jorge Rodriguez Navarro and the other, anonymous, reviewer(s) for their contribution to the peer review of this work. Primary handling editor: Alison Stoddart, in collaboration with the *Nature Synthesis* team.

Reprints and permissions information is available at www.nature.com/reprints.

Publisher's note Springer Nature remains neutral with regard to jurisdictional claims in published maps and institutional affiliations.

Open Access This article is licensed under a Creative Commons Attribution 4.0 International License, which permits use, sharing, adaptation, distribution and reproduction in any medium or format, as long as you give appropriate credit to the original author(s) and the source, provide a link to the Creative Commons license, and indicate if changes were made. The images or other third party material in this article are included in the article's Creative Commons license, unless indicated otherwise in a credit line to the material. If material is not included in the article's Creative Commons license and your intended use is not permitted by statutory regulation or exceeds the permitted use, you will need to obtain permission directly from the copyright holder. To view a copy of this license, visit http://creativecommons.org/licenses/by/4.0/.

© The Author(s) 2023